ELSEVIER

Dynamics of Atmospheres and Oceans
35 (2002) 299–325

dynamics of atmospheres and oceans

www.elsevier.com/locate/dynatmoce

Vortex–ridge interaction in a rotating fluid

L. Zavala Sansón*

Department of Physical Oceanography, CICESE, Ensenada, B.C., Mexico

Received 3 July 2001; received in revised form 1 December 2001; accepted 26 May 2002

Abstract

The evolution of barotropic vortices interacting with a topographic ridge on a f-plane is studied by means of laboratory experiments in a rotating tank and numerical simulations. The initial condition in all experiments is a cyclonic vortex created at a certain distance from the ridge. The results are presented in two main scenarios: (a) *weak interactions*, which occur at early stages of the experiments, when the vortex is far from the ridge, and thus weakly experiences the influence of the topography. In these situations, the vortex slowly drifts towards the ridge with a leftward inclination due to the ascending slope of the topography. Such a behaviour is similar to the "northwestern" motion of cyclones over a weak sloping bottom. The circular shape of the monopolar vortex is preserved. (b) *Strong interactions*, in which the vortex core reaches the ridge and presents a more complicated evolution. The cyclone "climbs" to the top of the topography and crosses to the other side. Once the vortex experiences the opposite slope, it moves backwards trying to return to the original side of the ridge. For strong enough vortices, this process may be repeated a number of times until the vortex is dissipated by viscous effects. During these interactions the shape of the vortex is strongly deformed and several filaments are produced. In some cases the vortex is cleaved in two parts when crossing the ridge, one at each side of it and moving in opposite directions.

Weak and strong interactions are numerically simulated by using a quasi-two-dimensional model. The results confirm that the vortex behaviour is governed by stretching and squeezing effects associated with changes in depth over the ridge and, at latter stages, by Ekman damping due to the solid bottom. The main results observed during strong interactions on a f-plane are also found on preliminar topographic β-plane experiments.

Keywords: Vortices; Topography; Rotating fluids; Ekman effects

* Present address: Department of Physical Oceanography, CICESE, P.O. Box 433844, 92143-4844 San Diego, CA, USA.
E-mail address: lzavala@cicese.mx (L. Zavala Sansón).

0377-0265/02/$ – see front matter © 2002 Elsevier Science B.V. All rights reserved.
PII: S0377-0265(02)00014-3

1. Introduction

The evolution of large scale vortices in the ocean and atmosphere is a fundamental problem in geophysical fluid dynamics. There are several processes affecting the evolution of such vortices, for instance, the influence of currents or jets, the effects associated with the Earth's curvature (β or γ-effects), or topographic variations. In this study, the influence of bottom topography on the motion and evolution of a barotropic vortex is examined. In particular, the interaction of a cyclonic vortex with a topographic ridge in a rotating system is studied by means of laboratory experiments and numerical simulations.

The motivation for this study originates from numerous geophysical situations, where bottom topography may play an important role in the evolution of planetary flows, subject to the Earth's rotation. In oceanographic applications, for instance, the transport of dynamical and thermodynamical properties between different regions of the oceans is often attributed to mesoscale eddies, which are able to travel long distances (compared with their size) while remaining a coherent structure. During their drift, vortices may interact with topographic features (canyons, sea-mounts, escarpments, etc.) and modify their trajectory and/or lose their coherence. The Agulhas rings, for instance, produced near the coast of South Africa (see, e.g. Byrne et al., 1995), are considered an important source of heat and salt from the Indian Ocean into the South Atlantic (de Ruijter et al., 1999). Some of these eddies, with a mean radius of 200 km, remain as a coherent structure as they travel through the South Atlantic and reach the Brasil Current. In some other cases, however, the decay or splitting of these vortices has been observed during their drift when they encounter the Walvis ridge or the Mid-Atlantic ridge (Schouten et al., 2000). Therefore, it is important to understand the role of variable bottom topography on their trajectory and evolution.

In the atmosphere, tropical cyclones also transport important physical properties such as heat and humidity during their drift. Zehnder (1993) and Zehnder and Reeder (1997) have pointed out the possible influence of the Sierra Madre, a large-scale mountain range in central México, on the drift of tropical cyclones formed either at the Mexican West coast (North-Eastern Pacific) or over the Gulf of México. In both cases, the studies suggest that cyclones are apparently deviated toward the Sierra Madre, thus approaching the continent. These observations are supported by sets of historical paths and numerical simulations based on simple physical models of the atmosphere. Although these types of studies are not conclusive, they strongly suggest the importance of large-scale topographic features, such as the Sierra Madre, on the evolution of distant vortex structures produced over the ocean.

A fundamental difference between geophysical flows and laboratory experiments reported here, is that density variations are always present in oceanic and atmospheric situations. The present study is restricted to homogeneous flows, however, since it intends to gain a better understanding of the fundamental mechanisms of flow–topography interaction starting from the simpler barotropic situation. Furthermore, the barotropic case has proven to be a useful tool for the study of oceanic (Dewar and Gailliard, 1994) and atmospheric (Zehnder, 1993; Zehnder and Reeder, 1997) situations. It has to be stressed, therefore, that the experimental and numerical models presented in this article are strongly simplified models of large-scale geophysical vortices. In addition, this study deals with non-isolated vortices (i.e. with single-signed vorticity), which might be another limitation for direct comparison with oceanic cases, where vortices tend to be isolated.

This study is further extended by using two-dimensional (2D) numerical simulations of the rotating tank experiments. Physically, it is assumed that the fluid moves in columns that remain always aligned parallel to the rotation axis (or to the local component of the Earth's angular velocity, in geophysical flows). The advantage of using a 2D formulation is that this approximation allows a much easier physical explanation of the behaviour of real three-dimensional flows, which is the aim of this study. In order to understand the experimental results, the simplicity of 2D models will be fully exploited.

There are some other studies on the vortex–ridge interaction closely related to the present one. The numerical simulations of Zehnder (1993) and Zehnder and Reeder (1997) were based on a barotropic model on a β-plane in order to study the motion of an atmospheric cyclone in the presence of an idealised range of mountains. Their main results showed that the presence of the ridge induces the vortex to slowly drift towards it. That behaviour, related with the ascending slope of the ridge, is experimentally verified in this study. On the other hand, van Geffen and Davies (1999) reported an extensive numerical study of a barotropic vortex interacting with a ridge on a β-plane. Later, those authors extended their results for vortices interacting with a north–south ridge or trough (van Geffen and Davies, 2000). Although the numerical methods in this paper are similar to those studies, the range of flow parameters used here (as well as in the laboratory experiments) is different, as shall be explained below. More complicated numerical simulations using a two-layer system have been performed by Kamenkovich et al. (1996) and Beismann et al. (1999), in which a vortex encountered a north–south topographic ridge.

In contrast with previous studies, which are mainly focused on numerical results, the present paper provides experimental evidence complemented with numerical simulations confirming and adding information on the vortex–ridge problem. Another important difference is that although mesoscale vortices are affected by latitudinal variations of the Coriolis parameter (β-effect), the f-plane case is studied as a first approximation. The aim is to completely isolate the effects of the topographic feature on the vortex behaviour without the interference of planetary Rossby waves. The vortex–ridge interaction on a β-plane is only briefly examined in order to show that the main results on the f-plane also apply in the presence of the β-effect. One more difference with previous studies is the inclusion of bottom friction in the present numerical simulations, which is unavoidable in laboratory experiments with a duration of an Ekman period, at least.

The results can be described in terms of two main scenarios, which depend on the distance between the vortex and the topography. Such flow scenarios shall be described as weak (vortices far from the ridge) and strong (vortices over the ridge) interactions. Although both types of scenarios are governed by the influence of the variable topography (producing stretching and squeezing effects), weak interactions are nearly inviscid, whereas strong interactions are also influenced by bottom friction effects. In general, the results show that the topographic ridge acts as an attractor during weak interactions, and as a barrier for strong interactions.

The rest of the paper is organised as follows. Section 2 contains the f-plane laboratory experiments. In Section 3, the governing equations and basic scales of the problem are presented. The f-plane experiments are numerically simulated in Section 4. Finally, Section 5 contains a discussion on weak and strong interactions, and a β-plane experiment is briefly examined.

2. Laboratory experiments

2.1. Experimental arrangement

The laboratory experiments were performed in a rectangular rotating tank ($L_x \times L_y = 150\,\text{cm} \times 100\,\text{cm}$) filled with fresh tap water at a mean depth H_0 between 18 and 24 cm. Fig. 1 shows a schematic view of the experimental set-up. In all cases the rotation rate of the tank was fixed at $\Omega = 0.5\ \text{rad s}^{-1}$, which corresponds with a Coriolis parameter $f_0 = 2\Omega = 1\ \text{s}^{-1}$. The experimental procedure consisted of setting the tank in rotation at the specified

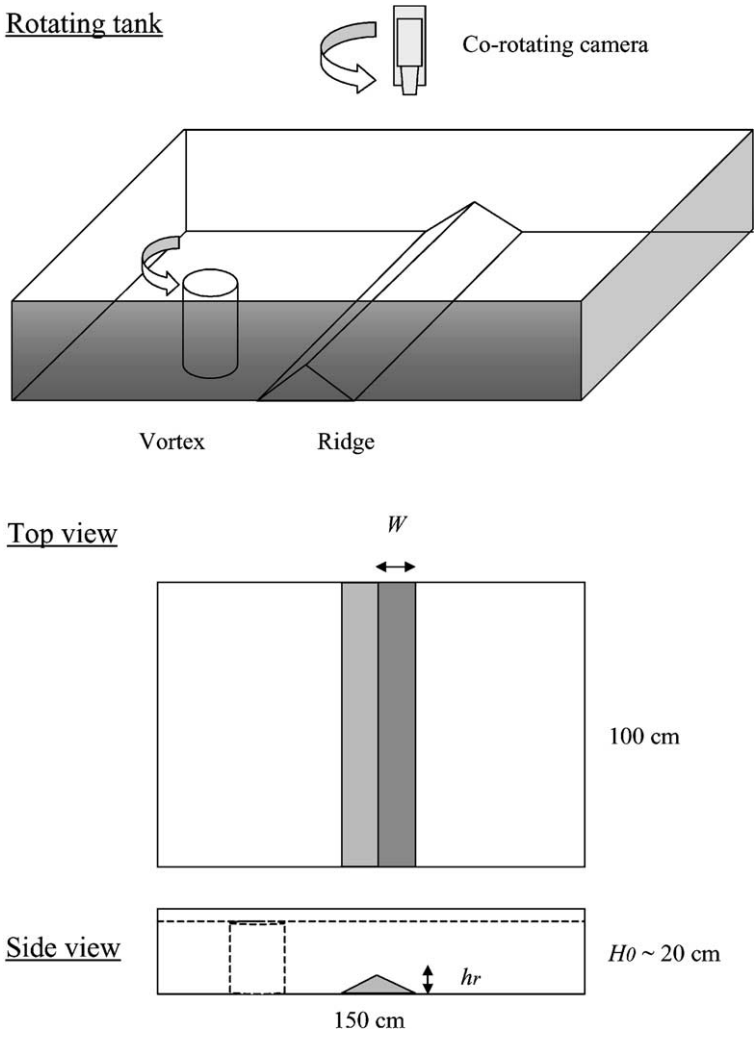

Fig. 1. Schematic view of the experimental arrangement. Cyclonic vortices are produced at the left-hand side (seen from above) of the triangle-shaped ridge.

constant angular speed about 30 min before the start of an experiment, in order to ensure that the fluid has reached a state of solid-body rotation (spin-up). Over the flat bottom of the tank, a triangle-shaped plate was fixed in order to simulate the topographic ridge. The ridge height was $h_r = 3$ cm and the (half) width W varied between 5 and 10 cm. The top of the ridge is at $x = 75$ cm and the edges are at $x_{left} = 75 - W$, and $x_{right} = 75 + W$ cm. It is anticipated here that changes in depth due to the ridge are much more important than the effects of the parabolic free surface, which will be ignored through the rest of the paper. This will be further supported by numerical simulations, which do not include free surface effects, showing the same tendency as the experiments.

In this study the well-known "sink" cyclonic vortices are used (see, e.g. Kloosterziel and van Heijst, 1992). Sink vortices are produced by locally syphoning a fixed amount of fluid ($\approx$ 3 l), during a certain period of time ($\approx$ 60 s), through a thin perforated tube, which extends over the fluid depth (see Fig. 2 in Zavala Sansón and van Heijst (2000a)). With this method it is possible to reproduce different initial conditions by syphoning different amounts of water. For the flat-bottom case it is found that, once the forcing is stopped, the vorticity and velocity distributions are well approximated by the following expressions:

$$\omega_{sink}(r) = \frac{\Gamma}{\pi R^2} \exp\left(\frac{-r^2}{R^2}\right), \tag{1}$$

$$v_{sink}(r) = \frac{\Gamma}{2\pi r}\left[1 - \exp\left(\frac{-r^2}{R^2}\right)\right], \tag{2}$$

where Γ is the vortex strength (per unit depth), R a horizontal length scale, and r is the radial distance to the centre of the vortex. From (1), the peak vorticity at the vortex core is $\omega_0 = \Gamma/\pi R^2$. Typical vortex parameters for the laboratory experiments discussed here are $\Gamma \approx 60$–100 cm^2 s^{-1} and $R \approx 2$–5 cm (thus $\omega_0 \approx 1$–5 s^{-1}). It is found empirically that the longer the forcing time the stronger the vortex (this observation coincides qualitatively with the solution for planar viscous flow induced by a line sink of fluid reported by Voropayev and Afanasyev (1991)) Initially, the vortices are intense [$\omega_0/f_0 \sim O(1)$] but gradually they decay due to lateral diffusion of momentum and bottom friction.

Sink vortices are suitable structures for this type of experiments since they are remarkably stable over a flat bottom and far from lateral boundaries. In such cases, these vortices remain nearly circular while decaying. This is a useful property when only topographic perturbations are studied, and when the influence of non-topographic perturbations (e.g. centrifugal instabilities) has to be avoided during the vortex evolution. Furthermore, sink vortices have a single-signed vorticity and are hence non-isolated. Such a structure allows the vortex to interact with the ridge even when it is initially placed at a large distance (compared with the vortex size) from the topographic feature.

The vortices were visualised by adding fluorescent dye into their core, and the subsequent evolution was recorded with a co-rotating camera mounted at some distance above the tank. On the other hand, particle streaks recordings were obtained by tracking passive tracers that were floating on the free surface. Using these images, it is possible to visualise the circulation over the entire domain, which is more difficult to achieve when only dye is used.

2.2. Weak and strong interactions

On a flat bottom and far from lateral boundaries a cyclonic sink vortex created at the centre of the tank remains there while decaying (see, e.g. Zavala Sansón and van Heijst, 2000b). One of the main results examined in this article is that, due to the presence of the topographic ridge, the vortex is forced to drift towards it. The vortex evolution during this interaction is a complex process even for the barotropic case on a f-plane, as will be shown here. For this reason the main results have been divided according to the following observed scenarios: first, the vortex behaviour is described when it is initially placed far from the ridge (i.e. when the vortex centre is situated at a distance of four to five times its own radius from the ascending slope of the topography) and therefore it experiences a *weak interaction*. In this case, the vortex preserves its form while slightly drifting towards the ridge. Second, a *strong interaction* is produced when the vortex approaches the ridge, crossing it one or more times while experiencing important deformations on its shape and, in some cases, splitting in two parts.

Fig. 2a shows a photograph of a cyclonic vortex, visualised with dark dye, during a weak interaction. Note that on the f-plane it is not relevant at which side of the ridge the vortex is created (in contrast with the β-plane, as explained in last section), and thus the initial position of the vortex was arbitrarily chosen at the left side, seen from above. Initially, the vortex weakly experiences the effect of the ridge and remains almost at the initial position during the forcing process. Once the vortex has been created, however, it starts to drift almost in a straight line towards the ridge and to the upper part of the photograph. Note from the figure that, as the vortex approaches the ridge, its shape is not disturbed and remains nearly circular. This motion corresponds with the "local northwest" imposed by the ascending slope of the ridge: the vortex drifts upslope and to the left, relative to that slope (see, e.g. Carnevale et al., 1991; Zavala Sansón and van Heijst, 2000a). In accordance with this result, even a far situated vortex may be attracted by a topographic feature such as the ridge. This initial behaviour is observed in all experiments, with slight differences due to the unavoidable error introduced when sink vortices are produced. On the other hand, when the vortex reaches the ridge its circular shape is deformed. This is shown, for instance, in Fig. 2b, in which all the initial flow parameters are similar but now using a wider ridge. In this case, the vortex acquires an elliptical shape as it climbs towards the top of the ridge. This stage is considered, therefore, as the beginning of a strong interaction, which shall be described in next subsection.

Fig. 3a and b show the trajectories of four sink vortices in the presence of the same ridge ($W = 10$ cm, $h_r = 3$ cm). The difference between both panels is the mean depth ($H_0 = 23$ and 18 cm, respectively). The position of the vortex centre is visually determined from the video images and plotted every 10 s, with an estimated error of 1 cm. Such a trajectory can be approximated when a compact structure of the vortex core is visualised, despite strong deformations over the ridge. The two vortices in Fig. 3a start at the same initial position while having a different initial strength (one of the vortices was forced during a longer period thus producing a stronger vortex). The weaker vortex moves almost in a straight line towards the ridge and to the left, until it is dissipated by viscous effects. In this case, the core of the vortex only experiences a weak interaction and it does not even reach the ridge. For the intense cyclone, in contrast, the component towards the ridge is increased and therefore

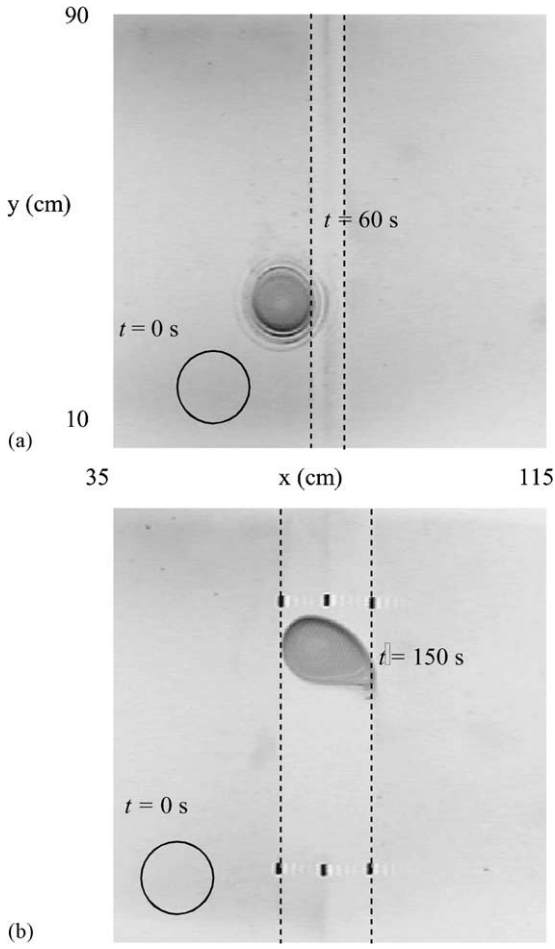

Fig. 2. Vortices approaching a ridge on the f-plane. The circle indicates the approximate size and position of the vortex at $t = 0$ s (i.e. when the forcing was stopped). Dashed lines show the edges of the ridge, which is centred at $x = 75$ cm. (a) Top view photograph of a cyclonic vortex during a weak interaction. The mean depth of the tank is $H_0 = 23$ cm; the ridge parameters are $h_r = 3$ cm and $W = 5$ cm. The initial vortex position is $x_0 = 60$ cm. (b) Top view photograph of a cyclonic vortex at the beginning of a strong interaction. The parameters are $H_0 = 18$, $h_r = 3$ cm, $W = 10$ cm, and $x_0 = 55$ cm.

the vortex interacts directly with the ridge, crossing to the other side of it. After crossing the top of the topography, however, the cyclone moves downwards, now due to the influence of the opposite slope (which imposes a new local "northwestern" direction). The vortex is not able to cross back to the left part of the domain due to the loss of strength, mainly by bottom viscous effects. Fig. 3b presents the trajectories of two vortices with similar strength but now created at a different initial position. As expected, the vortex far from the ridge experiences a weaker interaction and therefore it moves in a straight line towards the ridge and to the left, without reaching the topography. The vortex closer to the ridge, on the other

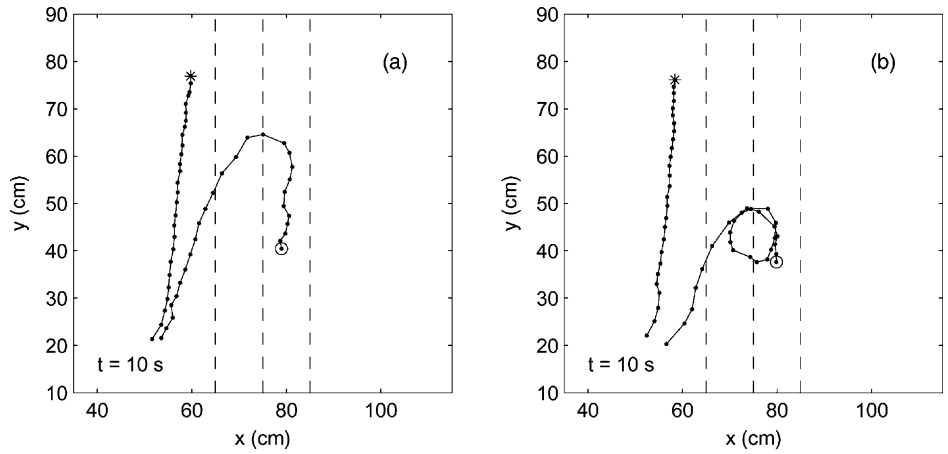

Fig. 3. Trajectories of four vortices from $t = 10$ to 270 s, every 10 s. The ridge parameters are $h_r = 3$ cm and $W = 10$ cm. (a) Two vortices with a different initial strength (i.e. created with a different forcing time) starting at the same initial position $x_0 = 50$ cm. The final positions are marked with $*$ and ○, for the weak and the intense vortex, respectively. The mean depth is $H_0 = 23$ cm. (b) Similar vortices (same forcing time) starting at a different initial position, $x_0 = 50$ cm and $x_0 = 55$ cm. The final positions are marked with $*$ and ○, respectively. The mean depth is $H_0 = 18$ cm.

hand, climbs the ascending slope and crosses from one side to the other a number of times before being dissipated.

Summarising, two types of vortex–ridge interaction have been defined: (a) weak interactions, in which vortices initially far from the ridge are induced to drift towards it (with a leftward component) almost in a straight line. The initial circular shape is nearly preserved. (b) Strong interactions, in which vortices climb the ridge while being deformed, and cross it one or more times. In the following subsections the vortex fate during strong interactions is described.

2.3. Vortices over the ridge

Fig. 4 presents the behaviour of the vortex whose trajectory was drawn in Fig. 3a during the strong interaction, that is, when it crosses the ridge and moves in the opposite direction. In this case, after the vortex has been attracted by the ridge, it shows a much more complicated evolution. At $t = 150$ s, the vortex is at top of the ridge and the shape becomes slightly elliptical, with the major axis perpendicular to the isobaths. When the vortex has crossed the ridge it is strongly deformed and the direction of motion is reversed, i.e. the vortex now moves according with the new local northwestern direction, imposed by the opposite slope, and tries to get back across the ridge. During this process part of its mass has been lost at the left side ($t = 190$–210 s). The formation of a thin filament at the right part of the vortex at $t = 190$ s is also very clear. For final stages of the experiment the vortex has been dissipated and the dyed fluid forms a long tendril distributed along the ridge ($t = 230$–270 s). Despite the strong deformation, the vortex core is still visible at these times.

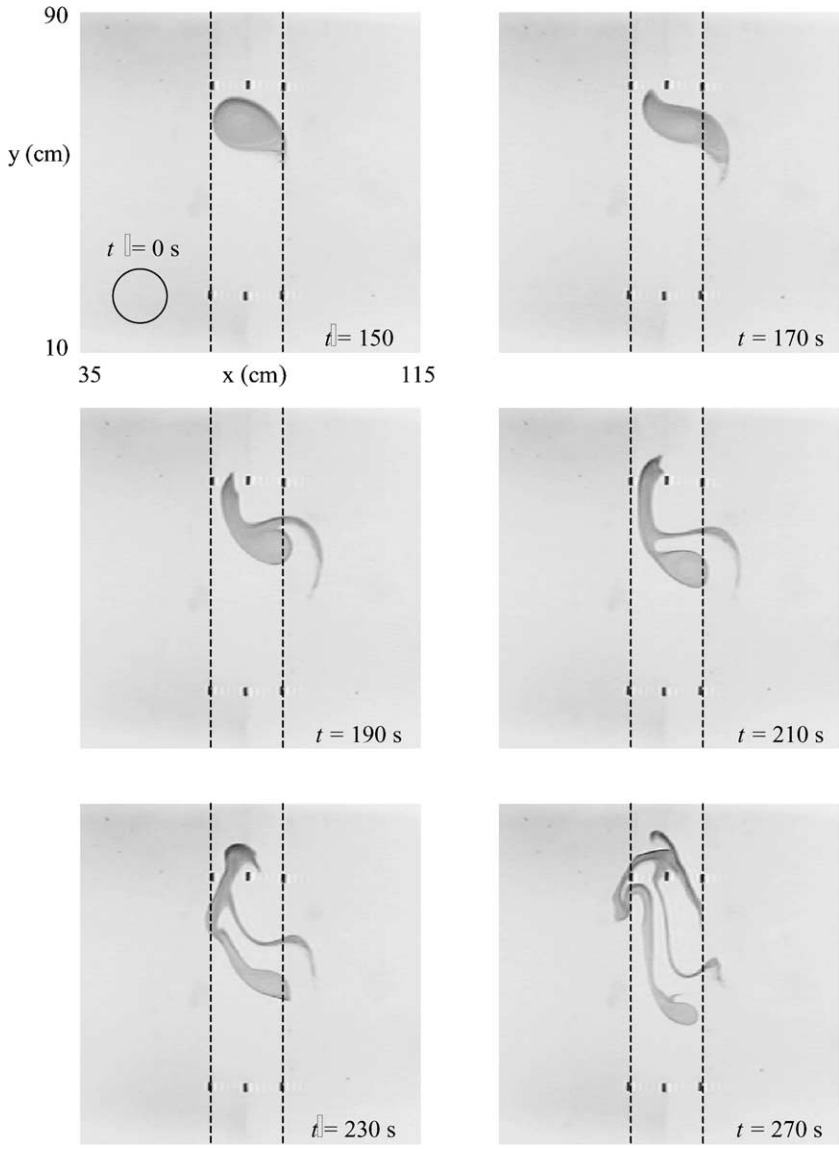

Fig. 4. Top view photographs showing the evolution of a vortex during a strong interaction on a f-plane. The parameters are $h_r = 3$ cm and $W = 10$ cm, $H_0 = 23$ cm and $x_0 = 50$ cm. The vortex trajectory, crossing the ridge one time, is plotted in Fig. 3a.

The vortex distortion can be understood by using the particle streaks recordings described above. In particular, it can be shown that the elliptical shape of the vortex, produced when it crosses the top of the ridge, is associated with the topographic Rossby radiation over the slopes of the topography. Fig. 5 shows the passive tracer streaks floating on the surface in

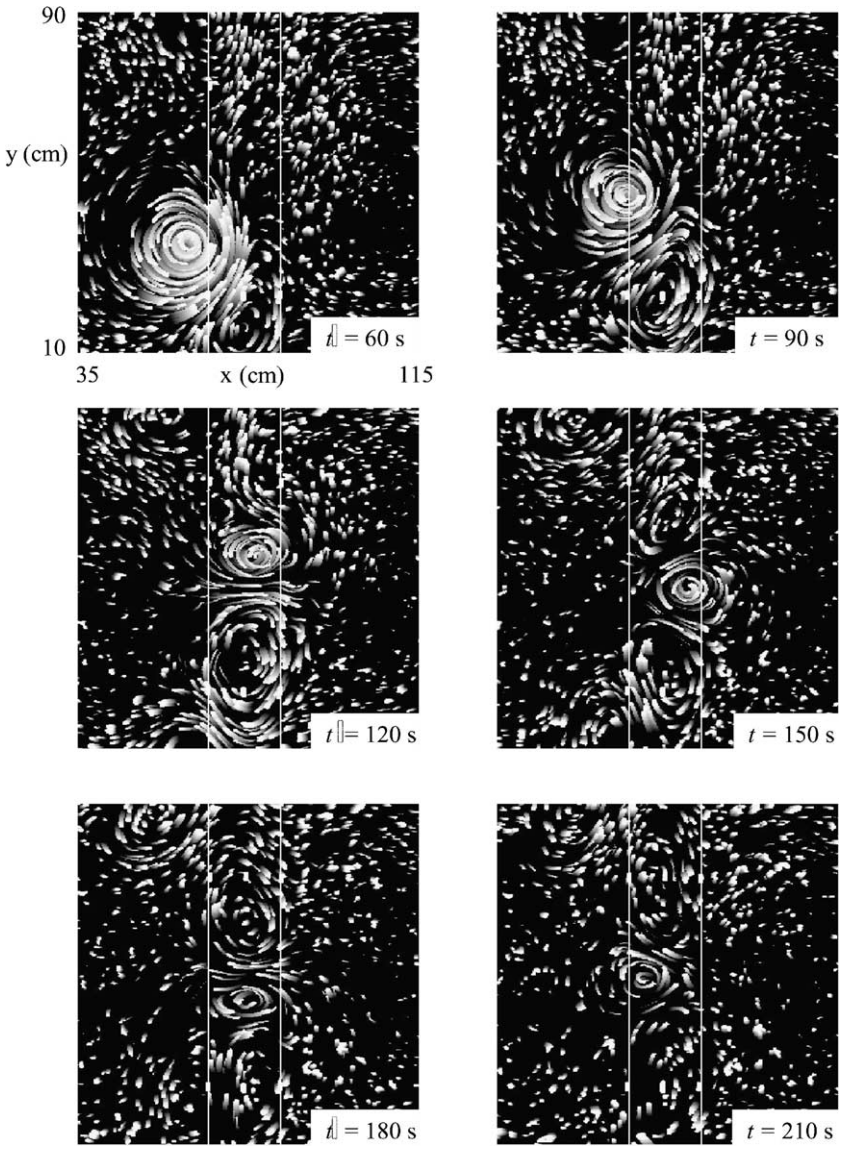

Fig. 5. Particle streak recordings of a cyclonic vortex during a strong interaction. White lines show the edges of the ridge. The elliptical deformation is produced after $t = 120$ s. The flow parameters are $h_r = 3$ cm, $W = 10$ cm, $H_0 = 21$ cm, $x_0 = 55$ cm, $\Gamma = 100\,\mathrm{cm^2\,s^{-1}}$ and $R = 2.5$ cm, approximately.

another experiment in which a strong interaction occurs. These plots reveal the formation of an opposite circulation cell (i.e. anticyclonic) formed over the ridge, below the vortex ($t = 60$–90 s). This cell, which starts the vortex elongation at $t = 120$ s, is associated with the topographic radiation induced by the slope, due to squeezing effects. Once the vortex has

crossed, it experiences the opposite slope of the ridge and a new circulation cell associated with the topographic radiation appears at the upper part ($t = 120$–150 s). The combination of these two anticyclonic cells produces the elliptical shape of the vortex when it is situated at top of the ridge, as clearly seen at $t = 180$ s. Also, the formation of filaments seems to

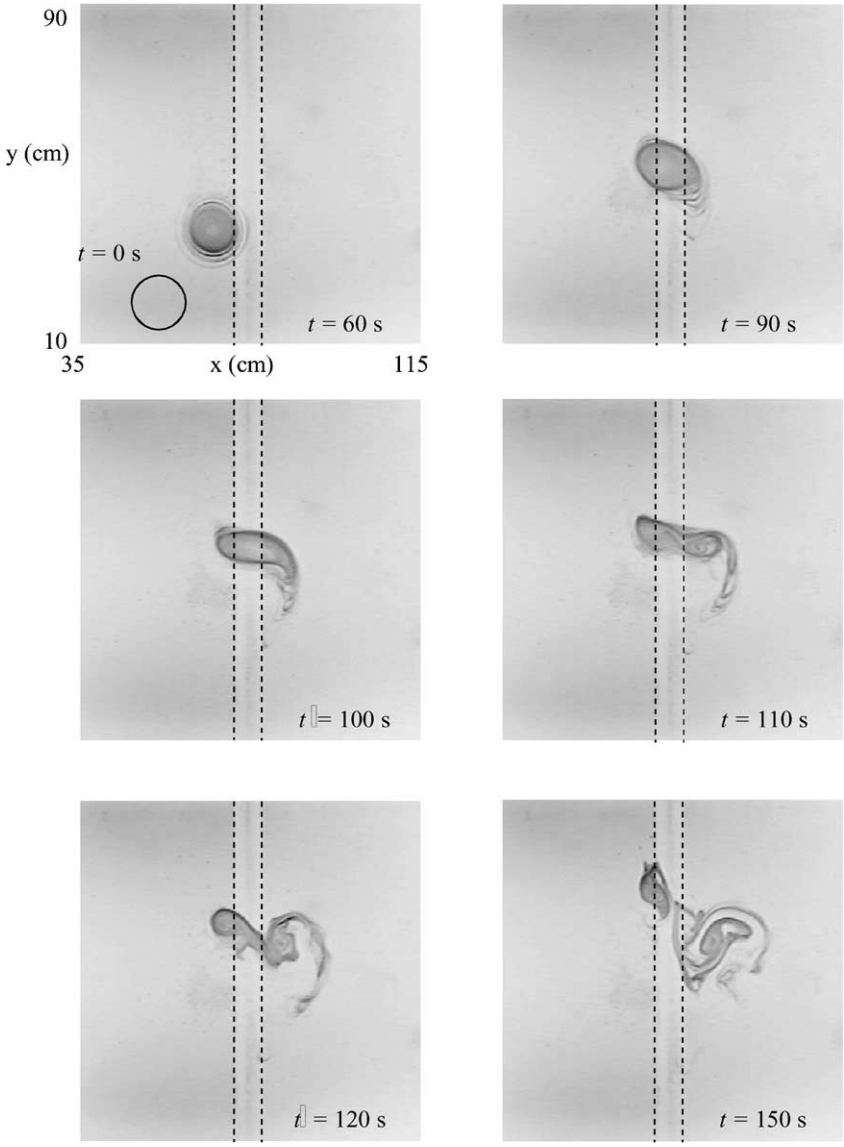

Fig. 6. Top view photographs showing the evolution of a vortex during a strong interaction over a narrow ridge. The vortex cleavage occurs at $t = 110$ s. The parameters are $h_r = 3$ cm and $W = 5$ cm, $H_0 = 21$ cm and $x_0 = 60$ cm.

be associated with this mechanism, although it is much more difficult to visualise from the presented photographs.

2.4. Vortex cleavage

The vortex deformation when crossing the topography leads to remarkable events, such as the vortex splitting in two parts, one at each side of the ridge. This effect is suggested by previous experiments when the vortex leaks part of its fluid as it crosses to the other side (see for instance Fig. 4 at $t = 210$ s). For certain flow parameters the vortex cleavage is more symmetric. Fig. 6 shows a sequence of photographs with the evolution of a vortex over a narrow ridge ($W = 5$ cm, $h_r = 3$ cm). The cyclone approaches the ridge and starts to cross it ($t = 90$ s), as in previous cases. A strong elliptical deformation is produced at $t = 100$ s. At this moment, part of the vortex experiences one slope of the ridge while the other part experiences the opposite slope. As a result, the vortex cleaves in two parts, each one moving in opposite directions under the influence of the corresponding slopes ($t = 120$ s). Note that both parts remain connected by a filament of dyed fluid. Afterwards, both of them are dissipated by bottom friction.

3. Governing equations

3.1. Physical model

It is assumed that the physical mechanisms involved in the experimental results described in last section are governed by the barotropic nondivergent vorticity equation (see, e.g. Grimshaw et al., 1994). This is a first approximation of the shallow water primitive equations for a homogeneous fluid layer over topography. This assumption has been justified by previous studies in which the experimental evolution of barotropic vortices over different bottom topographies have been successfully explained by using this model (see Zavala Sansón et al., 1999; Zavala Sansón and van Heijst, 2000a). Within this approximation the horizontal velocities (perpendicular to the axis of rotation) are assumed to be depth-independent, and free-surface effects are neglected in the continuity equation, which is equivalent to filtering out gravity waves.

Considering the f-plane approximation, the dynamic equation governing the fluid motion is

$$\frac{\mathrm{D}\omega}{\mathrm{D}t} + \left(\frac{\partial u}{\partial x} + \frac{\partial v}{\partial y}\right)(\omega + f_0) = \nu\nabla^2\omega, \tag{3}$$

where $\mathrm{D}/\mathrm{D}t = \partial/\partial t + \boldsymbol{u}\cdot\nabla$ is the material derivative, $\boldsymbol{u} = (u, v)$ the horizontal velocity vector with components in x (west-east) and y (south-north) directions, $\omega = (\partial v/\partial x) - (\partial u/\partial y)$ is the relative vorticity, ∇ is the horizontal gradient operator, and f_0 the Coriolis parameter. This expression is obtained by subtracting the cross-derivatives of the horizontal momentum equations. The continuity equation is

$$\frac{\partial(hu)}{\partial x} + \frac{\partial(hv)}{\partial y} = 0, \tag{4}$$

where $h(x, y) = H_0 - h_B(x, y)$ is the local fluid depth, H_0 is the undisturbed depth, and h_B the topography, which only depends on the spatial form of the bottom boundary. Note that, according with the rigid-lid approximation, free surface elevations have been neglected with respect to h_B. Thus, a function ψ can be defined by

$$hu = \frac{\partial \psi}{\partial y}, \qquad hv = -\frac{\partial \psi}{\partial x}. \tag{5}$$

Using these expressions, Eq. (3) is written in the $\omega - \psi$ formulation

$$\frac{\partial \omega}{\partial t} + J(q, \psi) = \nu \nabla^2 \omega, \tag{6}$$

where J is the conventional Jacobian operator and $q = (\omega + f_0)/h$ is the potential vorticity. From the definitions of the relative vorticity and stream function it is verified that

$$\omega = -\frac{1}{h}\nabla^2 \psi + \frac{1}{h^2}\nabla h \cdot \nabla \psi. \tag{7}$$

Note that Eq. (6) can be written as

$$\frac{Dq}{Dt} = \frac{\nu}{h}\nabla^2 \omega. \tag{8}$$

In the inviscid limit, $Dq/Dt = 0$, which expresses conservation of potential vorticity per fluid column.

The physical model given by (6) and (7) does not include Ekman damping effects associated with the bottom boundary layer. Bottom friction is expected to play an important role in the vortex evolution, however, since the duration of the laboratory experiments is relatively long (i.e. comparable with the Ekman period). In order to introduce bottom damping effects the model derived by Zavala Sansón and van Heijst (2002) is adopted. In that study the evolution equation is

$$\frac{\partial \omega}{\partial t} + J(q, \psi) - \frac{\delta_E}{2h}\nabla \psi \cdot \nabla q = \nu \nabla^2 \omega - \frac{\delta_E}{2h}\omega(\omega + f_0), \tag{9}$$

while the $\omega - \psi$ equation is given by

$$\omega = -\frac{1}{h}\nabla^2 \psi + \frac{1}{h^2}\nabla h \cdot \nabla \psi + \frac{\delta_E}{2h}\frac{2}{h^2} J(h, \psi), \tag{10}$$

where the thickness of the Ekman layer is

$$\delta_E = \left(\frac{2\nu}{f_0}\right)^{1/2}. \tag{11}$$

Note that the Ekman friction terms are proportional to $\delta_E/2h(x, y)$, which is a small number since the Ekman layer thickness is always much smaller than the fluid depth under typical experimental conditions, i.e. $\delta_E/2h \ll 1$. Assuming the ridge height to be small compared with the total depth yields $\delta_E/2h \approx \delta_E/2H_0 = E^{1/2}/2$, with E the Ekman number defined as

$$E = \frac{2\nu}{f_0 H_0^2}. \tag{12}$$

It should also be noticed that for moderate Rossby number, bottom friction effects are mainly due to the linear Ekman term in the right-hand side of Eq. (9).

3.2. Basic scales

Before presenting the numerical results, a scale analysis of the governing equations is carried out. The analysis consists of determining the nondimensional parameters that measure the production of relative vorticity per fluid column, as given by Eq. (3). This expression describes changes of vorticity due to horizontal divergence and lateral diffusion. In order to account for Ekman friction, the horizontal divergence can be written as

$$\frac{\partial u}{\partial x}+\frac{\partial v}{\partial y}=-\frac{1}{h}(\boldsymbol{u}\cdot\nabla h_{\mathrm{B}})+\frac{1}{2}E^{1/2}\omega, \tag{13}$$

where the last term represents the Ekman pumping from the thin Ekman layer at the solid bottom. The topographic variables are non-dimensionalised by using the total depth H_0, the halfwidth of the ridge W and its maximum height h_{r}, while the vorticity V/R is used for the last term (with V the typical azimuthal velocity of the vortex V, and R its length scale). This yields

$$\frac{\partial u}{\partial x}+\frac{\partial v}{\partial y}\sim\frac{Vh_{\mathrm{r}}}{H_0W}+\frac{1}{2}E^{1/2}\frac{V}{R}. \tag{14}$$

Thus, the nondimensional form of (3) is

$$\frac{\mathrm{D}\omega}{\mathrm{D}t}=\left(\frac{\beta_{\mathrm{r}}}{h}(\boldsymbol{u}\cdot\nabla h_{\mathrm{B}})+\frac{1}{2}E^{1/2}\omega\right)(\epsilon\omega+1)+\frac{\epsilon}{Re}\nabla^2\omega, \tag{15}$$

where the nondimensional numbers are:

$$\beta_{\mathrm{r}}=\frac{Rh_{\mathrm{r}}}{WH_0},\qquad \epsilon=\frac{V}{f_0R},\qquad Re=\frac{VR}{\nu}, \tag{16}$$

and the Ekman number E is given by (12). The flow divergence induced by the shape of the topography is proportional to both β_{r}, which simply represents the nondimensional form of the topographic β-effect associated with the slope of the ridge, and $E^{1/2}$, due to bottom damping. Note that both effects are coupled with the strength of the vortex, measured by the Rossby number ϵ. Lateral viscous effects are given by the inverse of the Reynolds number Re. Using typical orders of magnitude of the experimental flow parameters ($R\approx 5\,\mathrm{cm}$, $V\approx 2\,\mathrm{cm\,s^{-1}}$, $H_0\approx 20\,\mathrm{cm}$, $h_{\mathrm{r}}\approx 3\,\mathrm{cm}$, $W\approx 10\,\mathrm{cm}$, $f_0\approx 1\,\mathrm{s^{-1}}$, $\nu\approx 0.01\,\mathrm{cm^2\,s^{-1}}$) yields $\beta_{\mathrm{r}}\sim 0.075$, $\epsilon\sim 0.4$, $Re\sim 1000$, $E^{1/2}\sim 0.007$. Considering these values it can be concluded that the main changes of relative vorticity are due to topography effects, depending on β_{r}, and to linear Ekman friction. Bottom damping effects are manifested at times of order of the Ekman period, which is defined as

$$T_{\mathrm{E}}=\frac{2}{f_0E^{1/2}}. \tag{17}$$

Typical values are $T_{\mathrm{E}}\approx 285\,\mathrm{s}$, which is much longer than the rotation period $T=4\pi/f_0\approx 12\,\mathrm{s}$. Therefore, vortices are mainly affected by β_{r}, while slowly decaying due to $E^{1/2}$. Lateral viscosity plays a minor role in the experiments.

It is important to point out, however, that β_r is obtained by assuming that the core of the vortex is actually experiencing the slope of the ridge, which will not be the initial situation in the laboratory experiments, where the vortex is initially placed far from the ridge (i.e. during weak interactions). In other words, the β-effect produced by the ridge must be very weak as long as the vortex is far from it and, therefore, an alternative expression for β_r must be defined.

Using x_0 as the initial distance from the vortex centre to the ridge, such that $x_0 \gg R$, the new velocity scale introduced in the continuity equation (4) is $\Gamma/(2\pi x_0)$. It must be remarked that this value represents the velocity over the ridge induced by the vortex and, in general, it will be smaller than the approximate maximum velocity near the core, given by $\Gamma/(2\pi R)$, which can be used when scaling other terms in Eq. (3). By using these scales (and considering $\omega_0 \sim \Gamma/(\pi R^2)$ for the vorticity), Eq. (15) is obtained again but now the new parameter associated with the ridge is

$$\beta_r = \frac{R^2 h_r}{2x_0 W H_0}. \tag{18}$$

Apparently, this number is more appropriate for vortices initially placed far from the ridge, since it tends to zero for large x_0, i.e. for vortices which do not "feel" the topography. Furthermore, for $x_0 \sim R/2$ (when the vortex approaches the ridge) the original β_r parameter is recovered.

4. Numerical simulations

The numerical runs in this section simulate the laboratory experiments using a wider range of vortex and ridge parameters. The aim is to examine the importance of the flow parameters on the vortex evolution and to gain a better understanding on the physical processes involved. For clarity, the results for weak and strong interactions are presented separately.

In order to show the effects of variable topography without bottom friction the barotropic nondivergent vorticity model in the $\omega - \psi$ formulation, i.e. Eqs. (6) and (7), is solved by means of a finite differences code. This method was successfully used by Zavala Sansón et al. (1999), and Zavala Sansón and van Heijst (2000a), where experimental sink vortices interacting with different bottom topographies were numerically simulated. (Using a similar procedure, van Geffen and Davies (1999, 2000) included variable topography effects, without Ekman damping, in their numerical studies.) In contrast with previous authors, additional simulations with bottom friction effects are performed by solving Eqs. (9) and (10) with the same numerical scheme.

The numerical vortices are initialised by using expressions (1) and (2). The Coriolis parameter is taken as $f_0 = 1\ \mathrm{s}^{-1}$ and the kinematic viscosity as $\nu = 0.01\ \mathrm{cm}^2\,\mathrm{s}^{-1}$. The domain is a 150 cm $\times$ 150 cm square with no-slip boundary conditions, which is discretised by 129 $\times$ 129 grid points. This numerical domain is larger than the experimental rotating tank in order to avoid the influence of lateral boundaries on the initial motion of the vortex. The timestep is 0.1 s for all simulations.

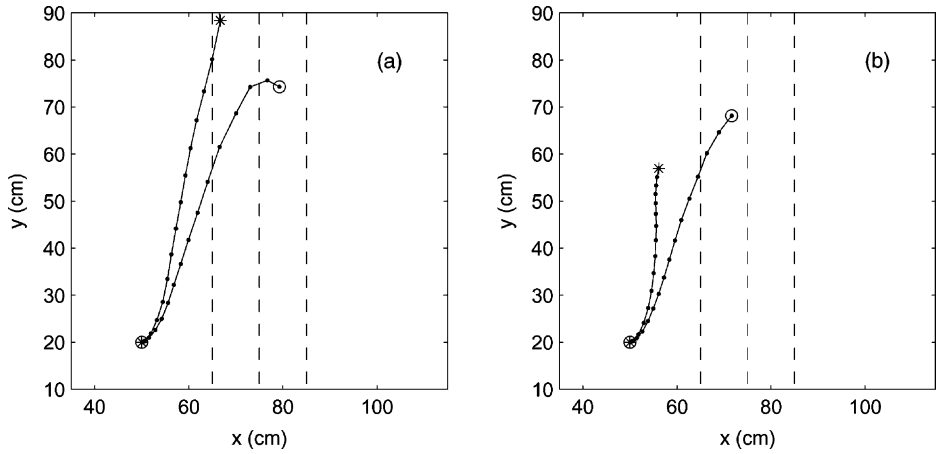

Fig. 7. Numerically calculated trajectories of a cyclonic vortex from $t = 0$ to 140 s, every 10 s, when the depth fluid is $H_0 = 12$ cm ($*$) and 18 cm ($\bigcirc$). (a) In the absence of bottom friction. (b) Including bottom friction. The vortex parameters are $\Gamma = 80\,\mathrm{cm^2\,s^{-1}}$ and $R = 2.5$ cm. The ridge parameters are $h_\mathrm{r} = 3$ cm and $W = 10$ cm.

4.1. Weak interactions

4.1.1. Relative height and bottom friction effects

Fig. 7a shows the trajectories of a cyclonic vortex when the fluid depth is $H_0 = 12$ and 18 cm. In both cases the ridge height is $h_\mathrm{r} = 3$ cm, that is, the relative height is $h_\mathrm{r}/H_0 = 1/4$ and $1/6$, respectively. The vortex position is dotted every 10 s (roughly every rotation period). Both simulations are based on Eqs. (6) and (7), which only consider changes in depth on fluid columns associated with the ridge, and a slow decay due to lateral viscous effects. From this figure it is observed that the vortex trajectory has a stronger attraction towards the ridge for greater H_0, while the vortex moves almost parallel to the ridge for smaller H_0. This motion is clearly associated with the β-effect due to the ascending slope of the ridge, which is proportional to the relative height h_r/H_0: the motion towards the local western direction (upper part of the figure) is enhanced for higher values of the topographic β_r, as shown in expression (16).

By comparing with trajectories in Fig. 3 during the same time span, it can be observed that in both situations the vortex drifts a larger distance than in the laboratory experiments. The main reason is the absence of bottom friction, which plays a role in the experiments by increasing the vortex decay. In order to account for bottom friction effects, both simulations are repeated, now based on Eqs. (9) and (10), and the results are plotted in Fig. 7b. The general tendency of both trajectories is clearly conserved: the cyclone with lower depth moves almost parallel to the ridge, while a greater H_0 implies a more pronounced drift towards the ridge, as in the case without bottom friction. The main difference with previous panel is that both vortices travel a shorter distance, and that the vortex with $H_0 = 12$ cm moves slower, due to a greater bottom dissipation. These trajectories are now comparable, qualitatively, with the observed paths during the experiments. Additional simulations using different fluid depths were carried out, showing similar results.

4.1.2. Vortex parameters

Fig. 8 shows the influence of the vortex parameters Γ and R in its trajectory towards the ridge. All simulations in this figure include Ekman damping. The left panel in Fig. 8a shows the trajectory of two vortices with initial $\Gamma = 60$ and $80\,\mathrm{cm^2\,s^{-1}}$, and the same length scale $R = 2.5\,\mathrm{cm}$. It is observed that the intense vortex has a greater attraction towards the ridge than the weak vortex. Eventually, the intense cyclone experiences a strong interaction, while the weak vortex travels a much shorter distance and it does not interact directly with the ridge. These results show that the trajectory is dependent on the vortex strength: as the vortex moves towards the topographic feature it may climb the ridge (strong vortices) or it may move almost parallel to it (weak vortices). The difference between both trajectories is associated with the larger flow velocity over the ridge produced by the strong vortex. This is shown at the right panel, where the initial radial velocity distributions are plotted. The secondary circulation induced by the variable topography is expected, therefore, to induce a greater influence on the upslope component of motion of the strong vortex.

From the previous figure it can be inferred that the important factor determining the trajectory is the external structure of the vortex (at $r \gg R$), i.e. the induced velocity over the ridge, and not the internal velocity distribution at the vortex core ($r \sim R$). This is clearly shown in Fig. 8b, where the trajectory of two vortices with same Γ and different length scale R (2 and 3.5 cm) are plotted. Although the inner structure is entirely different, as shown in the right panel, their trajectories are almost identical because the far field over the ridge is the same. In fact, the vortex paths only diverge when they directly interact with the ridge, more than 15 rotation periods later.

An additional result is shown in Fig. 8c, where the trajectories of two vortices with the same maximum azimuthal velocity but different R and Γ are plotted. As expected from previous observations, the stronger vortex has a greater attraction towards the ridge because the far velocity field over the topographic feature is larger in that case (see right panel). Such a vortex has a greater radius R too.

4.2. Strong interactions

When the vortex reaches the ridge a strong interaction occurs. It was shown in Fig. 4, for instance, that there may be complicated deformations of the vortex shape, such as the formation of filaments and long tendrils. This behaviour can be numerically reproduced, as shown in Fig. 9, where the calculated evolution of 500 passive tracers is presented. The tracers are initially placed around the vortex core, and their evolution is equivalent to the dye distribution in the laboratory experiments. This simulation can be qualitatively compared with the experiment of Fig. 4, in which the vortex crosses the ridge only once and it is dissipated at the right side of the topography. It is remarkable that the complicated dye distributions in the experiments are well reproduced during the simulation, namely, the initial deformation of the vortex ($t = 150$ and 170 s), and the formation of long filaments as the vortex experiences the effects of the opposite slope of the ridge ($t = 190$ and 210 s). This figure is a clear evidence that the flow remains nearly 2D, and that Eqs. (9) and (10) represent the physics of the problem very well. This is an important point when taking into account that the duration of the simulation was greater than an Ekman period ($T_\mathrm{E} \approx 255\,\mathrm{s}$), which is much longer than the rotation period of the system ($T \approx 12\,\mathrm{s}$).

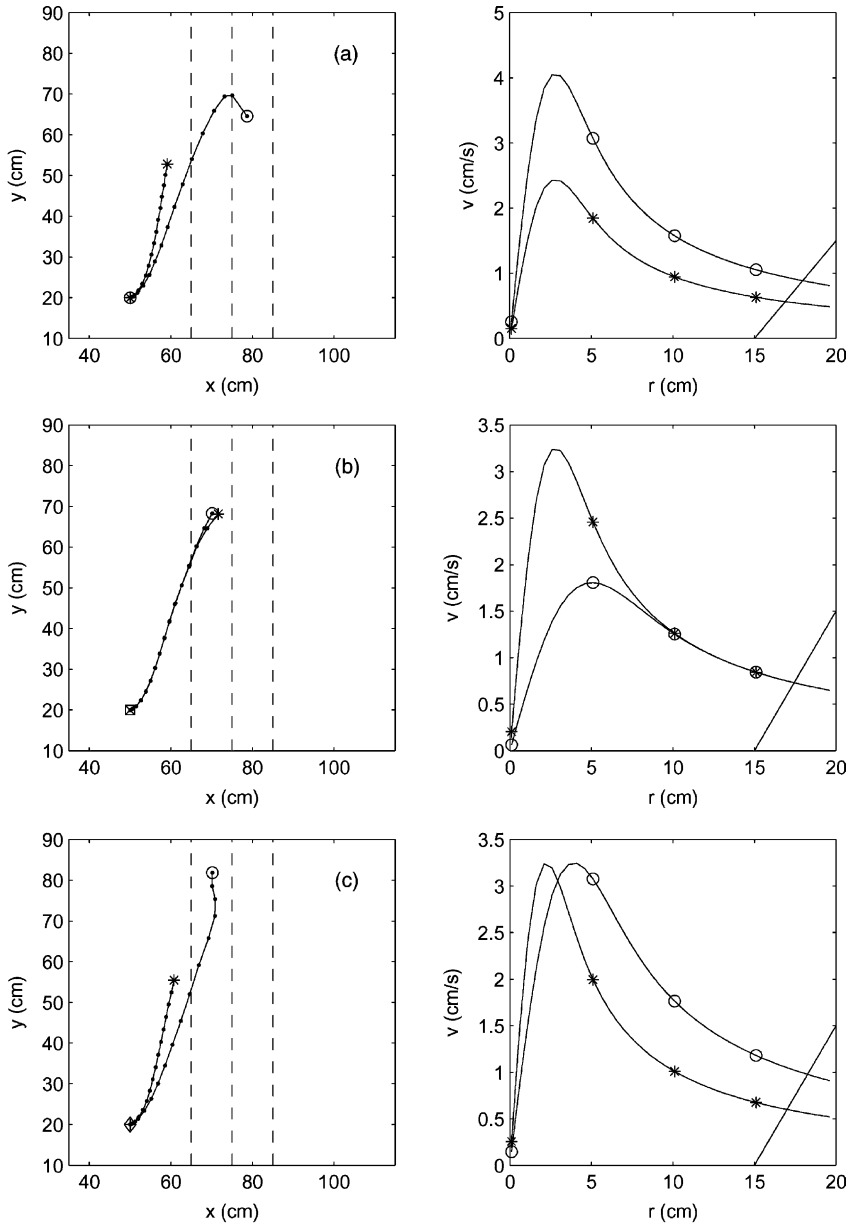

Fig. 8. Numerically calculated trajectories of two vortices with: (a) same length scale ($R = 2.5$ cm) and different strength ($\Gamma = 60$ and $100\,\mathrm{cm^2\,s^{-1}}$), marked with $*$ and ○, respectively. (b) Same strength ($\Gamma = 80\,\mathrm{cm^2\,s^{-1}}$) and different length scale ($R = 2$ and 3.5 cm), marked with $*$ and ○, respectively. (c) Same maximum velocity and different length scale ($R = 2$ and 3.5 cm) and strength ($\Gamma = 60$ and $80\,\mathrm{cm^2\,s^{-1}}$), marked with $*$ and ○, respectively. Left panels in all figures show the initial velocity profile. The inclined line indicates the edge of the ridge (with parameters $h_r = 3$ cm and $W = 10$ cm).

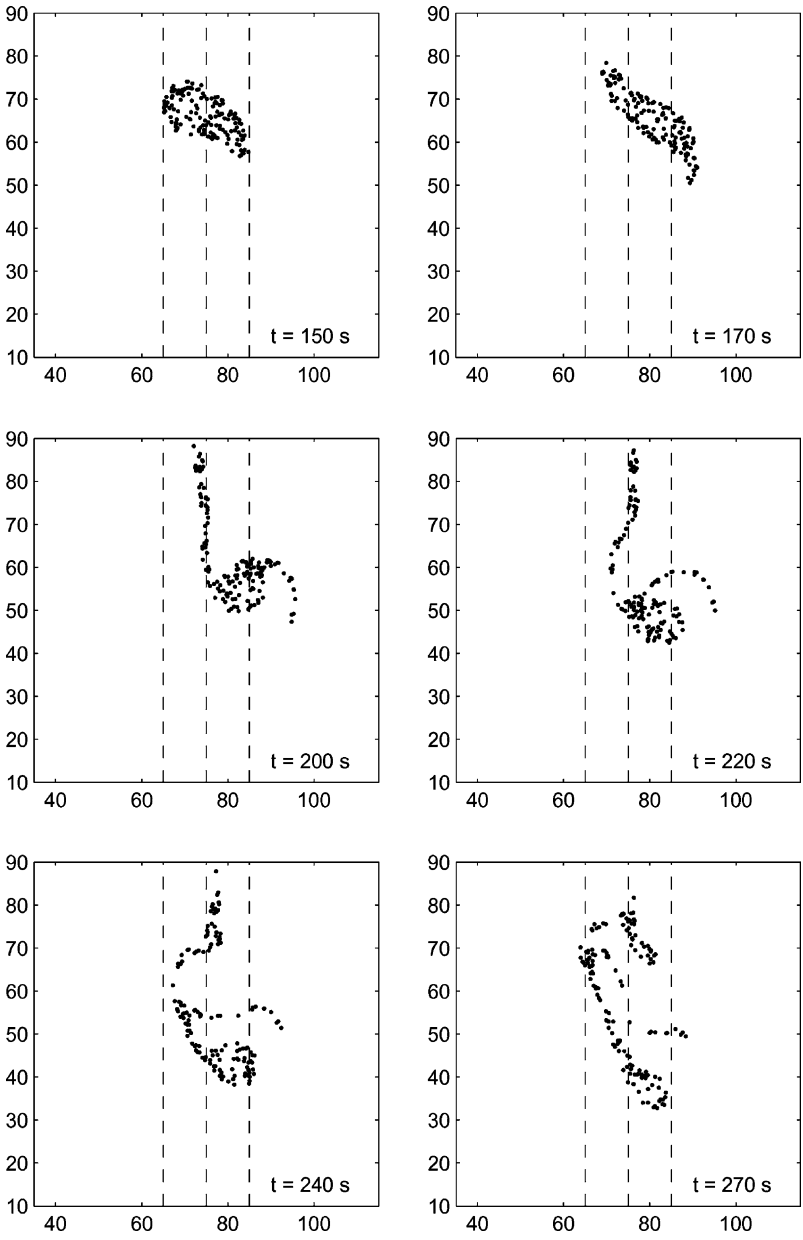

Fig. 9. Evolution of 500 tracers initially placed in a circle of radius 7 cm and centred at the vortex core, showing a strong interaction comparable with the experiment in Fig. 4. The flow parameters are: $H_0 = 18\,\text{cm}$, $h_r = 3\,\text{cm}$ and $W = 10\,\text{cm}$, $\Gamma = 80\,\text{cm}^2\,\text{s}^{-1}$, $R = 2.5\,\text{cm}$, $x_0 = 50\,\text{cm}$.

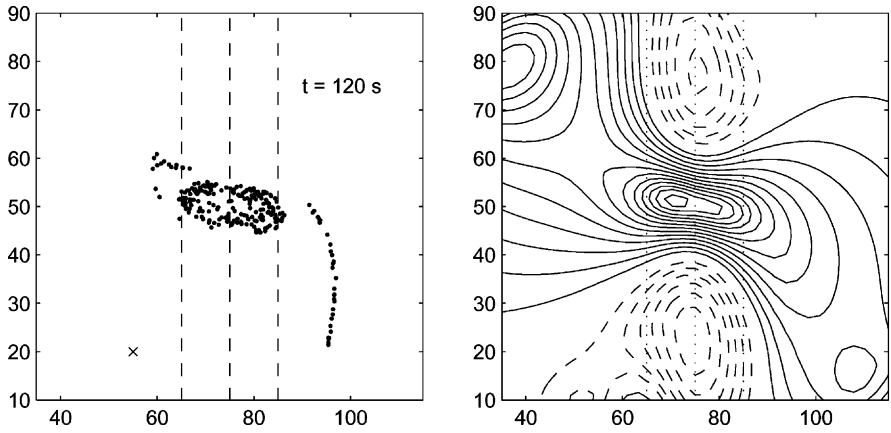

Fig. 10. Elliptical deformation of a vortex on top of the ridge at $t = 120$ s. The flow parameters are: $H_0 = 18$ cm, $h_r = 3$ cm and $W = 10$ cm, $\Gamma = 100\,\mathrm{cm^2\,s^{-1}}$, $R = 2.5$ cm, $x_0 = 55$ cm. Left panel shows 500 passive tracers initially placed in a circle of radius 7 cm and centred at the vortex core. Right panel presents stream function contours at $t = 120$ s.

On the other hand, consider the elliptical deformation of the vortex over the top of the ridge. This process is presented in Fig. 10, which shows the calculated evolution of passive tracers and stream function contours at $t = 120$ s in a numerical simulation with the same initial flow parameters as those in the experiment shown in Fig. 5. As explained in that case, the elliptical deformation is produced by the presence of an anticyclonic circulation cell over the ascending slope of the ridge, due to squeezing of fluid columns. After experiencing the opposite slope, another anticyclonic cell at the upper part of the vortex is formed. Thus, both circulations deform the vortex over the ridge producing its elliptical shape. The simulations confirm that the anticyclonic circulations appear as a consequence of squeezing of fluid columns ascending over the ridge.

When the elliptical shape of the vortex is very pronounced, the cyclone is split in two parts, each one of them moving in opposite directions over the slopes of the ridge. As an example, an almost symmetric cleavage is presented in Fig. 11, which shows vorticity contours and the corresponding evolution of 500 tracers at three different times. As argued before, the vortex cleavage takes place as a consequence of the elliptical elongation over the ridge, which causes that one part of the vortex is dominated by the influence of one of the slopes, while the other part experiences the opposite slope. As a result, the vortex is divided in two.

What are the conditions for the vortex splitting? It seems there may be several factors involved in this process. For instance, cleavage is produced when the vortex is able to reach the top of the ridge; this means that the vortex must be strong enough in order to climb the ascending slope, or that the along-ridge motion does not dominate the vortex drift. In contrast, the vortex must be weak enough when reaching the top of the ridge, otherwise it would simply cross it. It must be pointed out, however, that a strong vortex may cross back again over the ridge; in fact, cleavage may be presented after the vortex crosses the ridge a

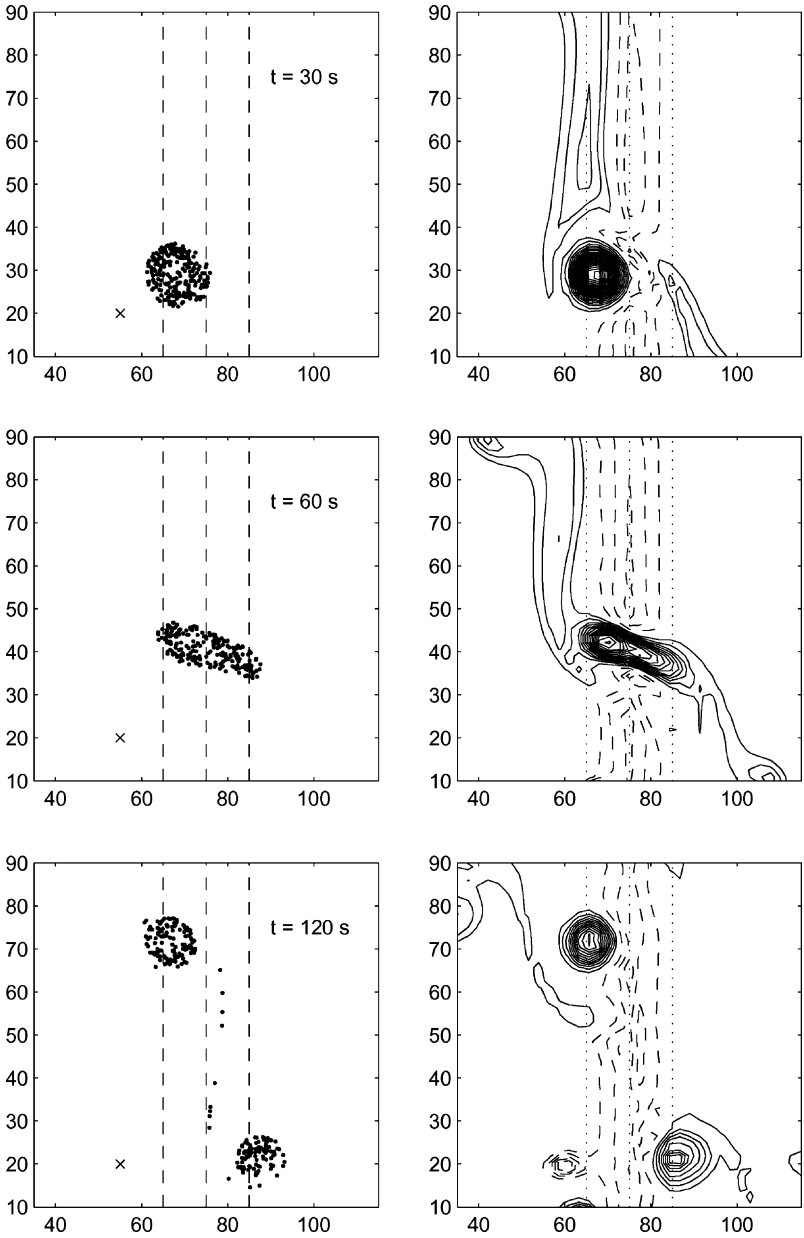

Fig. 11. Vortex cleavage during a strong vortex–ridge interaction. Left column shows the evolution of 500 tracers. Right column presents vorticity contours (with an interval of $0.1\,s^{-1}$). The flow parameters are: $H_0 = 18$, $h_r = 3$ and $W = 10\,cm$, $\Gamma = 120\,cm^2\,s^{-1}$, $R = 4.5\,cm$, $x_0 = 55\,cm$.

second or third time. Furthermore, strong slopes of the ridge (i.e. narrow ridges compared with the vortex size) will enhance the separation process of an elongated vortex over the top, because the β-effect experienced by both halves of the vortex will be more significant. This can be observed in Fig. 6, where the vortex over a narrow ridge is divided.

5. Discussion and conclusions

5.1. Weak and strong interactions

One of the main results during weak vortex–ridge interactions is the slow vortex drift towards the ridge. This effect is clearly produced by the ascending slope of the topography and is analogous to the topographic β-effect produced by a weak sloping bottom, in which the uphill (downhill) direction is equivalent with the northern (southern) direction on a β-plane, due to (quasi) conservation of potential vorticity. The "northwestern" motion of barotropic cyclones over a topographic slope has been studied experimentally by a number of authors (see, e.g. Carnevale et al., 1991; Zavala Sansón and van Heijst, 2000a), numerically and analytically (e.g. Grimshaw et al., 1994). It must be noticed, however, that those studies describe the vortex evolution over the slope, while in the present study, during weak interactions, the cyclone core is still far from the ridge. Even then, the vortex is induced to drift. This is a remarkable result, since it implies that a remote topographic feature may affect the vortex evolution due to the vorticity redistribution induced by the variable topography. A similar situation for vortices next to a topographic step was analytically described by McDonald (1998), and experimentally by Zavala Sansón et al. (1999). The self-propagation of a circular vortex subject to a small azimuthal perturbation on the f-plane was also discussed by Stern and Radko (1998) (this study, however, deals with isolated vortices).

The numerical results confirmed that the motion towards the ridge is enhanced for larger relative height h_r/H_0, which implies a steeper slope, and therefore larger values of β_r. It was also shown that the vortex structure at the core is not important for its trajectory, since such a motion is mainly determined by the far field induced by the vortex over the ridge. A difficult point to study is the influence of the width of the ridge on the vortex trajectory. The main reason for this uncertainty is that, for narrow ridges, it is expected that both slopes of the topography will play an important role. In this regard, several numerical simulations were performed without obtaining conclusive results.

Weak interactions may be important in atmospherical situations, as shown in the numerical studies of Zehnder (1993) and Zehnder and Reeder (1997), who have already pointed out the possible influence of the Sierra Madre in México on the trajectories of hurricanes, formed either at the Pacific Ocean or at the Gulf of México. The present results show that the presence of the ridge is sufficient to induce the motion of a non-isolated vortex even in the absence of the planetary β-effect or external flows, both imposed in most of the simulations of those authors. It is also worth noticing that, since non-isolated vortices propagate due to their far field interaction with the ridge, it is expected that isolated structures would have a less evident response to remote topography. This might be another limitation for oceanographical applications.

Strong interactions showed more complicated processes, as can be expected from considering that the opposite slope of the ridge will play a more important role in the vortex evolution. The vortex elongation and detrainment of fluid after each crossing is related with the topographic radiation due to both slopes as the vortex climbs and crosses the top of the ridge. This elliptical deformation is similar to the experimental results of Trieling et al. (1997), where the elongation of monopoles in a strain field was studied. In that study, the strain field is imposed externally, whilst in this study a similar forcing is developed by the anticyclonic circulation cells formed over the slopes of the ridge (due to squeezing effects). Another remarkable result is the vortex splitting, since it shows a mechanism by which the vortex fluid spreads in different directions.

5.2. *Inclusion of the β-effect*

An important factor for the evolution of large-scale flows is the latitudinal variation of the Coriolis parameter, the planetary β-effect. In these cases, vortices may drift due to β and eventually encounter a topographic feature. Here a laboratory experiment on a translating vortex on a topographic β-plane interacting with a ridge is briefly discussed.

The planetary β-effect is simulated in the laboratory by using a uniform, weak linear topography over the length of the tank. For this purpose a false bottom was used, which was lifted $\delta = 9$ cm at one of the ends of the tank, such that $\tan\gamma = \delta/L_y = 9/100$, i.e. a $\gamma \approx 5^\circ$ slope. This arrangement implies a constant Coriolis parameter f_0 and a smooth linear topography $H(y) = H_0 - y\tan\gamma$. It can be shown that this configuration, the topographic β-plane, is dynamically equivalent to a homogeneous fluid layer with a flat bottom on a β-plane (see, e.g. van Heijst, 1994). Such an arrangement has been used in a number of experimental studies (e.g. Carnevale et al., 1991; Zavala Sansón et al., 1999; Zavala Sansón and van Heijst, 2000a). The non-dimensional number measuring the "planetary" β-effect is:

$$\beta_{\mathrm{p}} = \frac{R\tan\gamma}{H_0}. \tag{19}$$

Using typical orders of magnitude for vortices in the laboratory, ($R \approx 5$ cm and $H_0 \approx 20$ cm) yields $\beta_{\mathrm{p}} \approx 0.02$. In addition to the weak overall topography, the triangle-shaped ridge used for the f-plane experiments (with $h_{\mathrm{r}} = 3$ cm, $W = 10$ cm, and $\beta_{\mathrm{r}} \approx 0.075$) was fixed along the "north–south" (shallow-deep) direction of the tank. The initial condition is a cyclonic, sink vortex created at the eastern side of the ridge, which moves northwestward, approaching the ridge (non-meridional ridges and/or vortices starting at the western side of the ridge are beyond the scope of this study).

Fig. 12 presents a sequence of photographs showing the vortex evolution when encountering the ridge. Initially the vortex tends to drift northwestward under the influence of the overall β-effect. However, the trajectory is soon deflected towards the south due to the local northwestern direction imposed by the ascending slope of the ridge ($t = 60$ s). The vortex crosses from one side to the other while deforming and producing filaments ($t = 90$–180 s). At $t = 210$ s, the vortex is strongly elongated on top of the ridge, and cleavage is produced at $t = 270$ s. It is observed that both sides of the vortex move in opposite directions since they experience the effect of opposite slopes. Finally, when motion has almost stopped due to viscous decay, both structures are deformed again over the top of the ridge ($t = 330$–360 s).

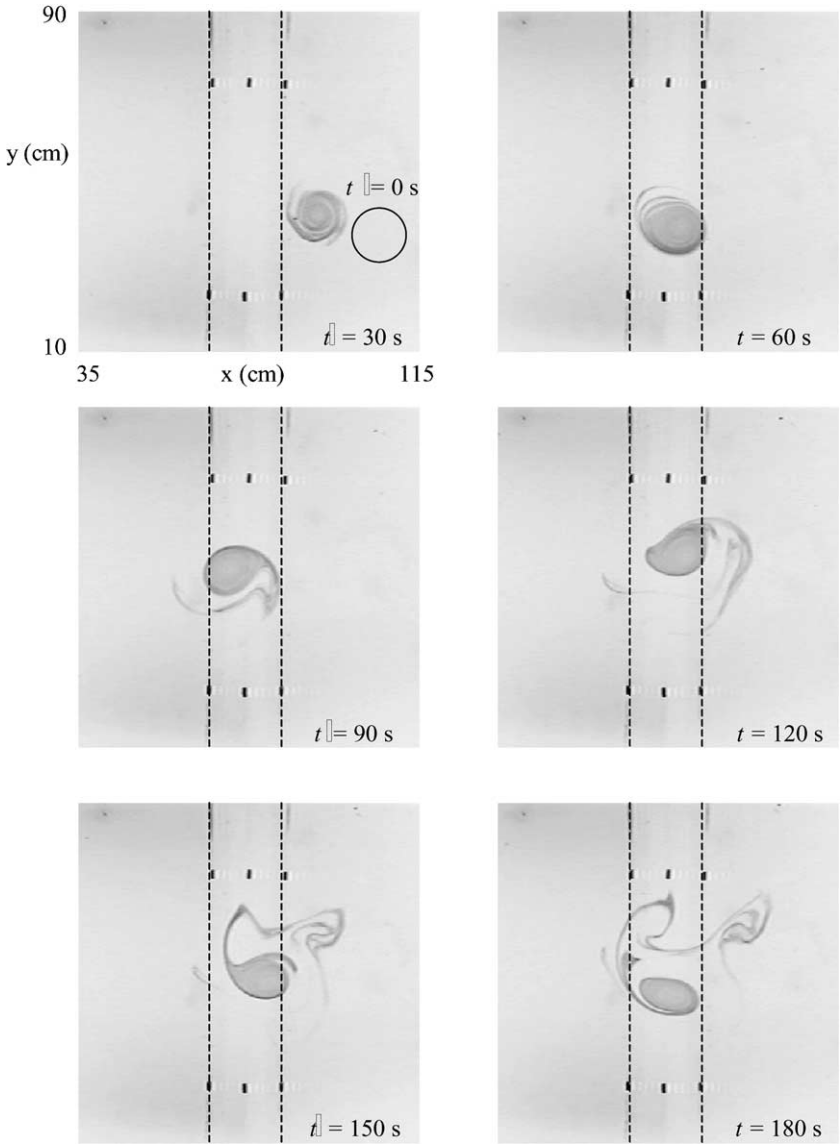

Fig. 12. Top view photographs showing the evolution of a vortex on a topographic β-plane. The initial position is at the eastern (right) part of the figure (x_0, $y_0 = 105, 40$) cm. The ridge parameters are $h_r = 3$ cm, $W = 10$ cm.

All these observations are very similar to those on the f-plane and therefore it may be concluded that, as long as the "planetary" β_p is smaller than the topographic β_r (that is, $\beta_p < \beta_r$), similar processes are expected to be observed in both planes. It is important to notice that the planetary effect is measured at all times by the parameter β_p given in (19). The β-effect induced by the ridge, in contrast, depends on the distance from the vortex to

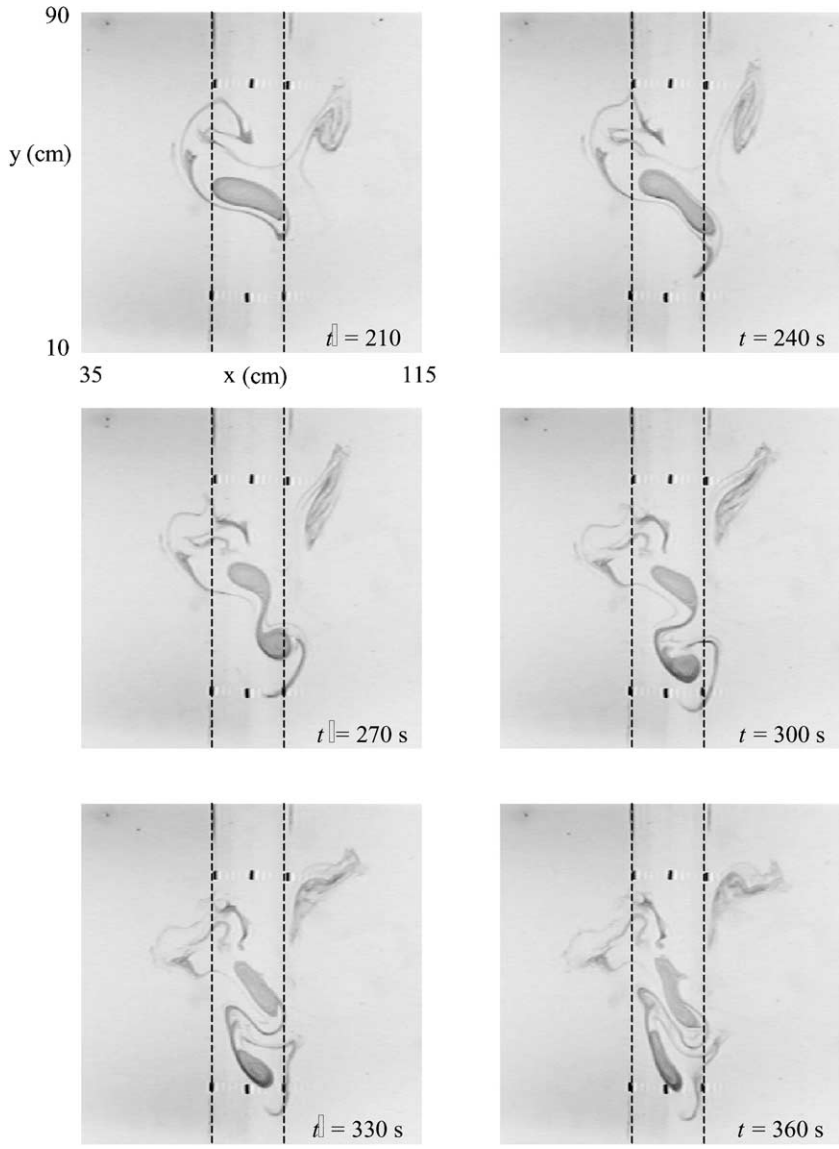

Fig. 12. (*Continued*).

the ridge: during weak interactions β_r is measured by (18) while for strong interactions it is better to use (16). The first case (large x_0) implies that $\beta_r < \beta_p$, which simply means that the vortex drift is dominated by the planetary effect as long as the vortex is far from the ridge. In contrast, during strong interactions it is found that $\beta_p < \beta_r$, which implies that the effect of the ridge dominates the vortex evolution. Therefore, it can be expected to find similar results on the f and β-planes during strong interactions.

An important difference between the present study and the numerical results of van Geffen and Davies (1999, 2000), is that those authors studied the opposite situation, that is, a strong planetary β-effect against a weaker topographic β due to the ridge, $\beta_p > \beta_r$. As a consequence, most of their vortices are able to cross the ridge and to continue a northwestward trajectory, "escaping" from the influence of the topography.

Acknowledgements

The author gratefully acknowledges financial support from the Consejo Nacional de Ciencia y Tecnología (CONACYT, México) and from Eindhoven University of Technology (TUE, The Netherlands) during the early preparation of this paper. The experiments were performed at the Fluid Dynamics Laboratory of TUE. Critical comments and conversations with G.J.F. van Heijst are sincerely appreciated.

References

Beismann, J.O., Kase, R.H., Lutjeharms, J.R.E., 1999. On the influence of submarine ridges on translation and stability of Agulhas rings. J. Geophys. Res. 104, 7897–7906.

Byrne, D.A., Gordon, A.L., Haxby, W.F., 1995. Agulhas eddies: a synoptic view using Geosat ERM Data. J. Phys. Oceanogr. 25, 902–917.

Carnevale, G.F., Kloosterziel, R.C., van Heijst, G.J.F., 1991. Propagation of barotropic vortices over topography in a rotating tank. J. Fluid Mech. 233, 119–139.

de Ruijter, W.P.M., Biastoch, A., Drijfhout, S.S., Lutjeharms, J.R.E., Matano, R.P., Pichevin, T., van Leeuwen, P.J., Weijer, W., 1999. Indian-Atlantic interocean exchange: dynamics, estimation and impact. J. Geophys. Res. 104, 20885–20910.

Dewar, W.K., Gailliard, C., 1994. The dynamics of barotropically dominated rings. J. Phys. Oceanogr. 24, 5–29.

Grimshaw, R., Broutman, D., He, X., Sun, P., 1994. Analytical and numerical study of a barotropic eddy on a topographic slope. J. Phys. Oceanogr. 24, 1587–1607.

Kamenkovich, V.M., Leonov, Y.P., Nechaev, D.A., 1996. On the influence of bottom topography on the Agulhas eddy. J. Phys. Oceanogr. 26, 892–912.

Kloosterziel, R.C., van Heijst, G.J.F., 1992. The evolution of stable barotropic vortices in a rotating free-surface fluid. J. Fluid Mech. 239, 607–629.

McDonald, N.R., 1998. The motion of an intense vortex near topography. J. Fluid Mech. 367, 359–377.

Schouten, M.W., de Ruijter, W.P.M., van Leeuwen, P.J., Lutjeharms, J.R.E., 2000. Translation, decay and splitting of Agulhas rings in the south-eastern Atlantic ocean. J. Geophys. Res. 105, 21913–21925.

Stern, M.E., Radko, T., 1998. The self-propagating quasi-monopolar vortex. J. Phys. Oceanogr. 28, 22–39.

Trieling, R.R., Beckers, M., van Heijst, G.J.F., 1997. Dynamics of monopolar vortices in a strain flow. J. Fluid Mech. 345, 165–201.

van Geffen, J.H.G.M., Davies, P.A., 1999. Interaction of a monopolar vortex with a topographic ridge. Geophys. Astrophys. Fluid Dyn. 90, 1–41.

van Geffen, J.H.G.M., Davies, P.A., 2000. A monopolar vortex encounters a north–south ridge or through. Fluid Dyn. Res. 26, 157–179.

van Heijst, G.J.F., 1994. Topography effects on vortices in a rotating fluid. Meccanica 29, 431–451.

Voropayev, S.I., Afanasyev, Y.D., 1991. Self-similar solution for the flow induced by a source/sink in a viscous rotating fluid. Mech. Res. Comm. 18 (4), 227–232.

Zavala Sansón, L., van Heijst, G.J.F., 2000a. Interaction of barotropic vortices with coastal topographies: Laboratory experiments and numerical simulations. J. Phys. Oceanogr. 30, 2141–2162.

Zavala Sansón, L., van Heijst, G.J.F., 2000b. Nonlinear Ekman effects in rotating barotropic flows. J. Fluid Mech. 412, 75–91.

Zavala Sansón, L., van Heijst, G.J.F., 2002. Ekman effects in a rotating flow over bottom topography. J. Fluid Mech., in press.

Zavala Sansón, L., van Heijst, G.J.F., Doorschot, J.J.J., 1999. Reflection of barotropic vortices from a step-like topography. Il Nuovo Cimento C 22, 909–929.

Zehnder, J.A., 1993. The influence of large-scale topography on barotropic vortex motion. J. Atmos. Sci. 50, 2519–2532.

Zehnder, J.A., Reeder, M.J., 1997. A numerical study of barotropic vortex motion near a large-scale mountain range with application to the motion of tropical cyclones approaching the Sierra Madre. Meteorol. Atmos. Phys. 64, 1–19.